We are IntechOpen, the world's leading publisher of Open Access books Built by scientists, for scientists

4,800
Open access books available

122,000
International authors and editors

135M
Downloads

Our authors are among the

154
Countries delivered to

TOP 1%
most cited scientists

12.2%
Contributors from top 500 universities

CLARIVATE ANALYTICS BOOK CITATION INDEX INDEXED

WEB OF SCIENCE™

Selection of our books indexed in the Book Citation Index in Web of Science™ Core Collection (BKCI)

Interested in publishing with us?
Contact book.department@intechopen.com

Numbers displayed above are based on latest data collected.
For more information visit www.intechopen.com

Chapter 27

Shunted Piezoceramics for Vibration Damping – Modeling, Applications and New Trends

Marcus Neubauer, Sebastian M. Schwarzendahl and Xu Han

Additional information is available at the end of the chapter

http://dx.doi.org/10.5772/50609

1. Introduction

Piezoelectric shunt damping is a well known technique to damp the vibrations of mechanical structures. This technique relies on the piezoelectric effect that converts mechanical energy into electrical energy. A damping effect on the host structure is observed when the electrical energy is dissipated. In order to optimize the damping performance, the transferred energy as well as the dissipated energy must be maximized. The transferred energy depends on the piezoelectric constants as well as the vibration mode and the location of the piezoelements within the structure. While higher piezoelectric constants generally increase the amount of transferred energy, the location can typically only be optimized for one eigenform of the structure. As a consequence, the piezoelectric transducer can be placed in such a way that it only affects one eigenform of the system. One measure for the coupling of the piezoceramics is the generalized coupling coefficient, which is defined for every vibration mode and generally takes different values for the individual modes. The design of the electrical shunt aims at maximizing the energy dissipation. Different networks have been developed, which can be classified into the categories passive, active, linear or non-linear. The best choice of network depends on the performance target, the availability of electrical power supply and the vibration behavior and excitation type of the mechanical structure.

Passive resonant circuits have been among the first networks for piezoelectric shunt damping. Forward studied inductance-resistance networks for the damping of optical systems [4] which were tuned to the resonant frequency of the mechanical system. Hagood and von Flotow then studied the performance and tuning of these *LR*-networks in more detail [7]. They described the shunted piezoceramics as a frequency depending stiffness and damping element and they showed the analogies of *LR*-shunted piezoceramics and tuned mass dampers. They obtained from calculations that the damping effect grows with the piezoelectric coupling coefficient. The standard *LR*-network can only be tuned to one frequency, therefore in the subsequent years new circuits were proposed that are capable to damp several frequencies at the same time [2, 9]. These networks basically consists of multiple *LR* branches that are tuned to the individual frequencies to be damped.

In order to enhance the limited damping performance of passive shuntings, active elements have been proposed. The mostly studied element is a negative capacitance, which can be realized by a negative impedance converter circuit [5]. Initially considered by Forward [3], a negative capacitance proves to be able to increase the effective piezoelectric coupling factor. Especially the combination of passive networks with active elements is a promising approach. This class of networks is called 'active-passive hybrid piezoelectric network' (APPN) by Tang [21]. Most prominent APPN networks are a negative capacitance with a resistor and a negative capacitance with an inductor and resistor.

The drawback of these linear resonant networks is that they all must be tuned to a certain frequency, which has to be known in advance and which should not change during operation. For many applications they are therefore not suitable. In these cases adaptive, non-linear networks are a better choice. The most common one is the 'synchronized switch damping on inductor' (SSDI) technique, which consists of an LR-branch and a switch that can connect and disconnect the network to the electrodes of the piezoceramics [10]. For the case of monoharmonic excitation the switch is closed at the moments of maximum deformation of the piezoceramics. In this moment, the electrical charge is inverted via the inductance. The inductance value is very small in order to realize a fast inversion. When fully inverted, the switch is closed so that the charge cannot flow anymore. During the following half period of excitation the charge stays nearly constant, so that the piezoceramics generates a force acting against the deformation velocity. The resulting force signal is nearly rectangular shaped. Like for the passive LR shunting the damping strongly depends on the electrical damping ratio, which can be set by the resistance value. A small damping results in a good inversion of the charge, which amplifies the stationary charge amplitudes and the dissipated energy. The adaptive capability of the SSDI technique comes from the triggering of the switching times. Therefore, typically one additional sensor is used which monitors the vibration of the mechanical structure. Due to this triggering, the force signal from the piezoceramics is always in phase with the structure vibration and the performance is only minimally dependend on the excitation frequency.

2. Modeling of mechanical structures with a shunted piezoceramics

In order to obtain general results which can be transferred to various mechanical structures, the structure is reduced to a one degree of freedom oscillator. The piezoceramics is shunted to an arbitrary electrical impedance Z, as shown in Figure 1. The equations of motion for this general case read

$$\begin{bmatrix} m & 0 \\ 0 & 0 \end{bmatrix} \begin{bmatrix} \ddot{q} \\ \ddot{Q} \end{bmatrix} + \begin{bmatrix} d & 0 \\ 0 & 0 \end{bmatrix} \begin{bmatrix} \dot{q} \\ \dot{Q} \end{bmatrix} + \begin{bmatrix} c + \frac{\alpha^2}{C_\mathrm{p}} & \frac{\alpha}{C_\mathrm{p}} \\ \frac{\alpha}{C_\mathrm{p}} & \frac{1}{C_\mathrm{p}} \end{bmatrix} \begin{bmatrix} q \\ Q \end{bmatrix} = \begin{bmatrix} F(t) \\ -u_\mathrm{p} \end{bmatrix}, \tag{1}$$

where the parameters m, d and c denote respectively the modal mass, damping and stiffness. Stiffness c is herein the sum of the mechanical stiffness c_mech and the stiffness of the piezoelement c_p. $F(t)$ represents the external force, u_p is the voltage at the electrodes of piezoceramics, C_p the capacitance of the piezoceramics and α the force factor which can be deduced from geometry and characteristics of the piezoceramics and the mechanical structure. The variables q and Q are respective the modal displacement and electrical charge.

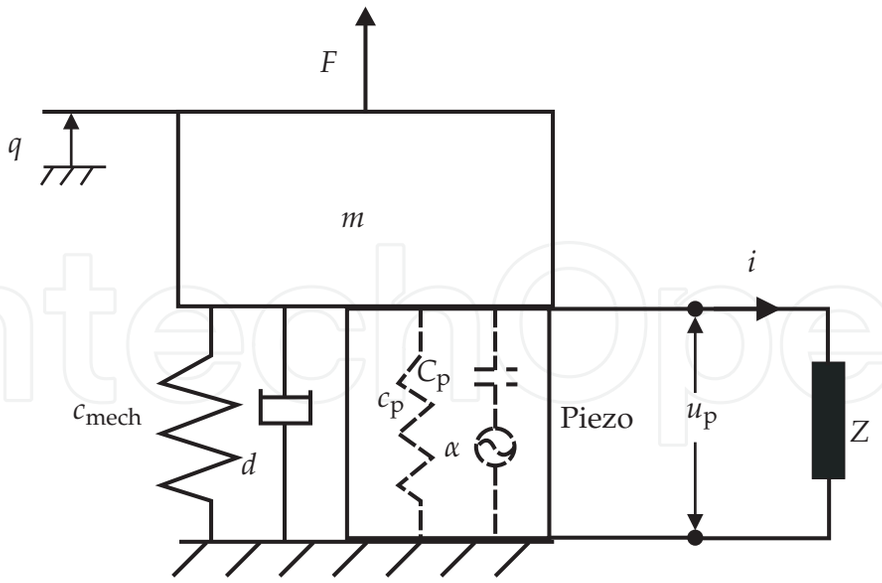

Figure 1. Single Degree-of-Freedom oscillator with piezoceramics and shunt circuit.

When the piezoceramics is shunted to an electrical circuit, the voltage u_p depends on the charge Q as well as the impedance Z of the shunt,

$$u_p = ZQ. \tag{2}$$

In this context, Z describes the relationship between voltage and charge rather than between voltage and current. Inserting (2) into (1), the generalized equation of a shunt damping system reads as

$$\begin{bmatrix} m & 0 \\ 0 & 0 \end{bmatrix} \begin{bmatrix} \ddot{q} \\ \ddot{Q} \end{bmatrix} + \begin{bmatrix} d & 0 \\ 0 & 0 \end{bmatrix} \begin{bmatrix} \dot{q} \\ \dot{Q} \end{bmatrix} + \begin{bmatrix} c + \frac{\alpha^2}{C_p} & \frac{\alpha}{C_p} \\ \frac{\alpha}{C_p} & \frac{1}{C_p} + Z \end{bmatrix} \begin{bmatrix} q \\ Q \end{bmatrix} = \begin{bmatrix} F(t) \\ 0 \end{bmatrix}. \tag{3}$$

This equation is the basis for all further calculations.

3. Optimization of resonant LR-shunting for damped mechanical systems

Let us first consider a resonant LR-shunt with impedance $Z = Ls^2 + Rs$. Substituting this term into (3) leads us to

$$\begin{bmatrix} m & 0 \\ 0 & L \end{bmatrix} \begin{bmatrix} \ddot{q} \\ \ddot{Q} \end{bmatrix} + \begin{bmatrix} d & 0 \\ 0 & R \end{bmatrix} \begin{bmatrix} \dot{q} \\ \dot{Q} \end{bmatrix} + \begin{bmatrix} c + \frac{\alpha^2}{C_p} & \frac{\alpha}{C_p} \\ \frac{\alpha}{C_p} & \frac{1}{C_p} \end{bmatrix} \begin{bmatrix} q \\ Q \end{bmatrix} = \begin{bmatrix} F(t) \\ 0 \end{bmatrix}. \tag{4}$$

For maximum damping performance the circuit parameters L and R have to be tuned in such a way that the system has double eigenvalues. For the undamped case $(d = 0)$ the optimal parameters are well known.

With the help of normalized, non-dimensional parameters, the equations can be written in a more compact form. In detail, the generalized piezoelectric coupling coefficient K, the eigenfrequency of the system with isolated electrodes ω_{iso}, the electrical eigenfrequency ω_{el},

the electrical damping ratio ζ_0 of the LR-branch and the frequency ratio η_{el} are introduced,

$$K^2 = \frac{\alpha^2}{cC_\mathrm{p} + \alpha^2}, \quad \omega_{\mathrm{el}} = \sqrt{\frac{1}{C_\mathrm{p} L}}, \quad \omega_{\mathrm{iso}}^2 = \frac{c + \alpha^2 / C_\mathrm{p}}{m},$$

$$\zeta_0 = \frac{R}{2}\sqrt{\frac{C_\mathrm{p}}{L}}, \quad \eta_{\mathrm{el}} = \frac{\omega_{\mathrm{el}}}{\omega_{\mathrm{iso}}} = \sqrt{\frac{m}{\alpha^2 L}} K. \tag{5}$$

The generalized piezoelectric coupling coefficient K is a measure of the effectiveness of the piezoceramics. It depends on the piezoceramics characteristics as well as on the structure vibration form. The shunt parameters L, R are substituted by non-dimensional parameters $\eta_{\mathrm{el}}, \zeta_0$. The matrix $\mathbf{A}$ of the corresponding state-space system then reads as

$$\mathbf{A} = \begin{bmatrix} 0 & 0 & 1 & 0 \\ 0 & 0 & 0 & 1 \\ -1 & -K^2 & 0 & 0 \\ -\eta_{\mathrm{el}}^2 & -\eta_{\mathrm{el}}^2 & 0 & -2\eta_{\mathrm{el}}\zeta_0 \end{bmatrix}, \tag{6}$$

and the characteristic equations become

$$\det\left(\mathbf{A} - \lambda \mathbf{I}\right) = \lambda^4 + 2\zeta_0\eta_{\mathrm{el}}\lambda^3 + \left(1 + \eta_{\mathrm{el}}^2\right)\lambda^2 + 2\zeta_0\eta_{\mathrm{el}}\lambda + \left(1 - K^2\right)\eta_{\mathrm{el}}^2 = 0. \tag{7}$$

Double eigenvalues are obtained when the shunt parameters are tuned according to

$$\eta_{\mathrm{el,opt}} = \frac{1}{\sqrt{1 - K^2}} \approx 1, \quad \zeta_{0,\mathrm{opt}} = K. \tag{8}$$

These equations basically state that the inductance has to be tuned in such a way that the electrical resonant frequency nearly equals the mechanical resonant frequency. The damping ratio of the circuit must match the generalized piezoelectric coupling coefficient K. The resulting damping ratio from such a shunting then becomes

$$D = \frac{K}{2\sqrt{1 - K^2}} \approx \frac{K}{2}. \tag{9}$$

This equation proves the importance of the generalized piezoelectric coupling coefficient K, as the damping performance grows with K. Figure 2 shows the influence of the network parameters upon the location of the complex eigenvalues.

For the damped mechanical oscillator, the same strategy can be followed to optimize the system. Normalizing the mechanical damping by $D_\mathrm{m} = \frac{d}{2m\omega_{\mathrm{iso}}}$ the characteristic equation of the system becomes

$$\lambda^4 + \left(2\zeta_0\eta_{\mathrm{el}} + 2D_\mathrm{m}\right)\lambda^3 + \left(1 + \eta_{\mathrm{el}}^2 + 4\zeta_0\eta_{\mathrm{el}}D_\mathrm{m}\right)\lambda^2 + \left(2\zeta_0\eta_{\mathrm{el}} + 2\eta_{\mathrm{el}}^2 D_\mathrm{m}\right)\lambda + \left(1 - K^2\right)\eta_{\mathrm{el}}^2 = 0. \tag{10}$$

The results for the optimal network parameters $\eta_{\mathrm{el,opt}}$ and $\zeta_{0,\mathrm{opt}}$ as well as the resulting damping performance are very lengthy terms. It is useful to express them in a Taylor series,

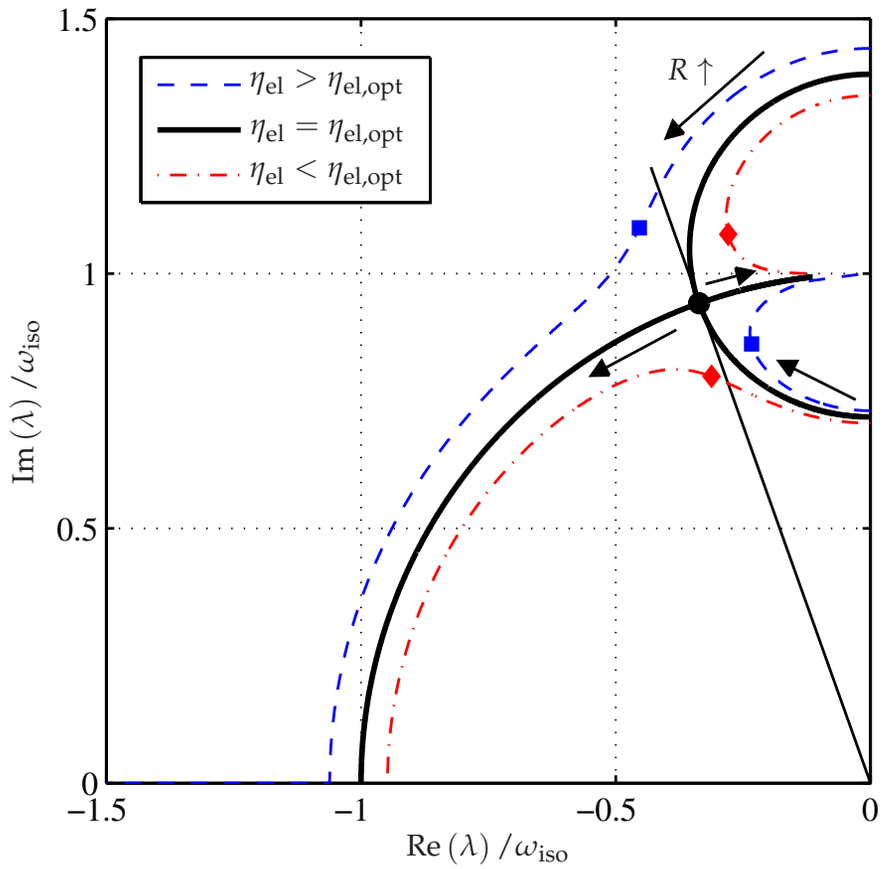

Figure 2. Eigenvalue of mechanical 1 DOF oscillator with *LR*-shunted piezoceramics.

and only consider the first elements of the series. This gives

$$\eta_{\mathrm{el,opt}} \approx \frac{1}{\sqrt{1-K^2}} + \frac{K}{1-K^2} D_{\mathrm{m}},$$

$$\zeta_{0,\mathrm{opt}} \approx K + \sqrt{1-K^2} D_{\mathrm{m}},$$

$$D \approx \frac{1}{2} \frac{K}{\sqrt{1-K^2}} + \frac{4-3K^2}{4-4K^2} D_{\mathrm{m}}. \tag{11}$$

These approximations are valid for small mechanical damping ratios D_{m}, which is practically fulfilled in most cases. The equations clearly show the trend when mechanical damping is included. For the undamped case, $D_{\mathrm{m}} = 0$, the results are per definition equal to the values obtained in (8) and (9). But additional mechanical damping leads to a slight increase of the optimum electrical resonant frequency η_{el} and damping ratio $\zeta_{0,\mathrm{opt}}$. Naturally also the resulting damping performance grows with additional mechanical damping. One can realize that for high mechanical damping D_{m} (compared to the coupling coefficient K), the overall damping converges the mechanical damping, $D \approx D_{\mathrm{m}}$, and the additional damping caused by the shunted piezoceramics is negligible.

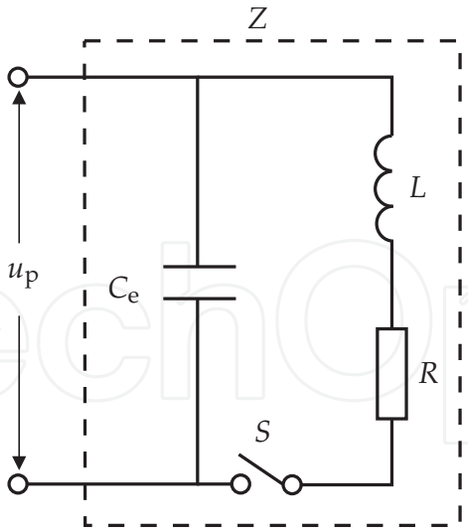

Figure 3. SSDNCI network.

4. Synchronized switch damping on negative capacitance and inductance (SSDNCI)

This section describes a novel combination of a negative capacitance together with the well-known SSDI-technique schematized in Figure 3, which has recently also been studied by other research groups [11]. It is intended to combine the adaptive ability of the SSDI with the enhanced performance and coupling of a negative capacitor. Again the calculations will be performed using nondimensional parameters,

$$\delta = \frac{C_e}{C_p}, \quad \omega_{el} = \frac{1}{\sqrt{(1+\delta)LC_p}}, \quad \zeta = \sqrt{1+\delta}\frac{R}{2}\sqrt{\frac{C_p}{L}} = \sqrt{1+\delta}\zeta_0, \quad \tau = \omega_{el}t. \tag{12}$$

The electrical damping ratio of the LR-branch of the circuit is again termen ζ_0, while the overall electrical damping ratio with negative capacitance is ζ. The capacitance ratio δ can be set by choosing appropriate values for the negative capacitance. For a positive external capacitance, the parameter δ is positive, for a negative capacitance it is negative. The electrical resonance frequency as well as the electrical damping ratio both depend on the capacitance ratio ζ. Setting $\delta = 0$ results in the standard SSDI technique without negative capacitance, with the corresponding electrical damping ratio ζ_0. Obviously, the negative capacitance influences the electrical resonance frequency as well as the damping ratio. Especially the latter one is important, as the damping ratio should be as small as possible. Using a negative capacitance reduces the damping ratio.

The switching network is a nonlinear system, but it can be considered as linear during the periods with open and closed switch. When the switch is closed, the shunt impedance Z_{cl} reads

$$Z_{cl} = \frac{1}{\frac{1}{Ls^2+Rs} + \frac{1}{1/C_e}} = \frac{Ls^2 + Rs}{C_eLs^2 + C_eRs + 1}. \tag{13}$$

Substitution of Z_{cl} into (3) and representation in terms of the non-dimensional parameters yields

$$\begin{bmatrix} m & 0 \\ \alpha\delta L & (1+\delta)L \end{bmatrix} \begin{bmatrix} \ddot{q} \\ \ddot{Q} \end{bmatrix} + \begin{bmatrix} 0 & 0 \\ \alpha\delta R & (1+\delta)R \end{bmatrix} \begin{bmatrix} \dot{q} \\ \dot{Q} \end{bmatrix} + \begin{bmatrix} c+\frac{\alpha^2}{C_{\mathrm{p}}} & \frac{\alpha}{C_{\mathrm{p}}} \\ \frac{\alpha}{C_{\mathrm{p}}} & \frac{1}{C_{\mathrm{p}}} \end{bmatrix} \begin{bmatrix} q \\ Q \end{bmatrix} = \begin{bmatrix} F(t) \\ 0 \end{bmatrix}. \tag{14}$$

The standard SSDI network without negative capacitance is the special case with $\delta = 0$.

In this study, a harmonic mechanical vibration q is assumed, and the influence of the shunted piezoceramics upon the vibration is neglected. This is fulfilled in good appromixation for systems where the piezoelectric coupling is not excessively large. Therefore, the second equation from (14) can be rewritten, summarizing all terms with q as excitation on the right side,

$$(1+\delta)L\ddot{Q} + (1+\delta)R\dot{Q} + \frac{1}{C_{\mathrm{p}}}Q = -(\alpha\delta L\ddot{q} + \alpha\delta R\dot{q} + \frac{\alpha}{C_{\mathrm{p}}}q). \tag{15}$$

When the switch is open, the piezoceramics is connected to the negative capacitance, $Z_{\mathrm{iso}} = \frac{1}{C_{\mathrm{e}}}$. Inserting this impedance into (3) yields

$$\begin{bmatrix} m & 0 \\ 0 & 0 \end{bmatrix} \begin{bmatrix} \ddot{q} \\ \ddot{Q} \end{bmatrix} + \begin{bmatrix} c+\frac{\alpha^2}{C_{\mathrm{p}}} & \frac{\alpha}{C_{\mathrm{p}}} \\ \frac{\alpha}{C_{\mathrm{p}}} & \frac{1}{C_{\mathrm{p}}}+\frac{1}{C_{\mathrm{e}}} \end{bmatrix} \begin{bmatrix} q \\ Q \end{bmatrix} = \begin{bmatrix} F(t) \\ 0 \end{bmatrix}. \tag{16}$$

The charge Q is directly coupled with mechanical displacement q. During the switch open period, the charge Q changes according to

$$Q(t) = -\frac{\alpha}{C_{\mathrm{p}}}\frac{1}{\frac{1}{C_{\mathrm{p}}}+\frac{1}{C_{\mathrm{e}}}}q(t) + C = -\alpha\frac{\delta}{1+\delta}q(t) + C, \tag{17}$$

where C is the offset of charge signal, which still has to be determined. For a harmonically excited system, it can be calculated by assuming that the voltage signal is periodic with the same period time. It is therefore sufficient to consider one half period time of excitation only. Every half period consists of a period of open switch and of closed switch. Here the magnitude change of switch open circuit and switch closed circuit are defined respectively as ΔQ_{open} and $\Delta Q_{\mathrm{close}}$. The steady state is then characterized by

$$\Delta Q_{\mathrm{open}} + \Delta Q_{\mathrm{close}} = 0. \tag{18}$$

This equation basically means that the voltage is the same after each period time. In the case of harmonic excitation with an amplitude of $\hat{q}$ and excitation frequency of Ω, the mechanical displacement, velocity and acceleration can be expressed as

$$q(t) = \hat{q}\cos(\Omega t), \quad \dot{q} = -\hat{q}\Omega\sin\Omega t, \quad \ddot{q} = -\hat{q}\Omega^2\sin\Omega t. \tag{19}$$

The change of charge ΔQ_{open} is proportional to the change in displacement during switch open period. With the absolute charge value after inversion (which is the initial condition of the closed switch period) termed Q_0, and the absolute value before inversion Q^*, we can write

$$\Delta Q_{\text{open}} = Q_0 - Q^* = -2\alpha\frac{\delta}{1+\delta}\hat{q},$$
$$Q_0 = \frac{1}{2}\Delta Q_{\text{open}} + C = -\alpha\frac{\delta}{1+\delta}\hat{q} + C. \tag{20}$$

Compared to the mechanical periodic time, the electric periodic time is normally very short. Additionally, the switching occurs at the times when the deformation q is maximized, which means that the velocity is zero. It is demonstrated in [14], that it is therefore feasible to neglect the change of mechanical signals during the time the switch is closed. Thus we can approximate the right side of (15) with the following terms: $q(t) = \hat{q}\cos(\Omega t) \approx \hat{q}$, $\dot{q} = -\hat{q}\Omega\sin(\Omega t) \approx 0$, $\ddot{q} = -\hat{q}\Omega^2\cos\Omega t \approx -\hat{q}\Omega^2$. As a result, the right side of the differential equation becomes a constant,

$$(1+\delta)L\ddot{Q} + (1+\delta)R\dot{Q} + \frac{1}{C_p}Q = \alpha\hat{q}(\delta L\Omega^2 - \frac{1}{C_p}). \tag{21}$$

The solution of (21) is the superposition of the general solution and the particular solution. The particular solution can be obtained with the Duhamel integral. After some mathematical calculations, the value of charge at τ^*, which is the moment of opening the switch, is obtained as

$$Q(\tau^*) = -e^{-\pi\zeta}Q_0 - \alpha\hat{q}(1+e^{-\pi\zeta}), \quad Q^* = |Q(\tau^*)|. \tag{22}$$

The difference between Q^* and Q_0 is the magnitude change of charge for closed switch ΔQ_{close}. Combining all results, the stationary value of charge Q_0 and the constant component C are obtained as

$$Q_0 = \alpha\hat{q}(\frac{1+e^{-\pi\zeta}}{1-e^{-\pi\zeta}} - \frac{2\delta}{1+\delta}\frac{1}{1-e^{-\pi\zeta}}), \quad C = \frac{1}{1+\delta}\alpha\hat{q}\frac{1+e^{-\pi\zeta}}{1-e^{-\pi\zeta}}. \tag{23}$$

The results for C and Q_0 are the absolute values, their signs periodically change so that they are always in antiphase with the velocity $\dot{q}$. Further on, this result can be approximated for low damping $\zeta \ll 1$,

$$C \approx \frac{1}{1+\delta}\alpha\hat{q}\frac{2}{\pi\zeta} = (1+\delta)^{-\frac{3}{2}}\alpha\hat{q}\frac{2}{\pi\zeta_0}. \tag{24}$$

Equation (24) demonstrates that the stationary charge is increased for $\delta < 0$, which means that only a negative capacitance increases the charge buildup. Especially when δ approaches -1, the constant C is theoretically infinity. The negative capacitance is an active analog circuit, so in practice the stationary charge cannot be infinitely high due to the limited maximal output of the operational amplifier. Additionally, the overall capacitance has to be positive in order to keep the electrical network stable. Therefore, the theoretical available range of the negative capacitance is the same as for the *LRC* shunt circuit

$$-C_p < C_e < 0 \quad \text{or} \quad -1 < \delta < 0. \tag{25}$$

The time signals of the SSDI and the SSDNCI with different capacitance ratios are given in Figure 4. For a clear illustration of the switching times t_{cl} and t_{op}, the inversion of charge does not occur instantaneously, as it is assumed in the calculations. Obviously, a larger negative capacitance increases the charge amplitudes as compared to the SSDI technique ($\delta = 0$).

Finally, the dissipated energy E_{diss} per vibration period, which is a measure of the damping

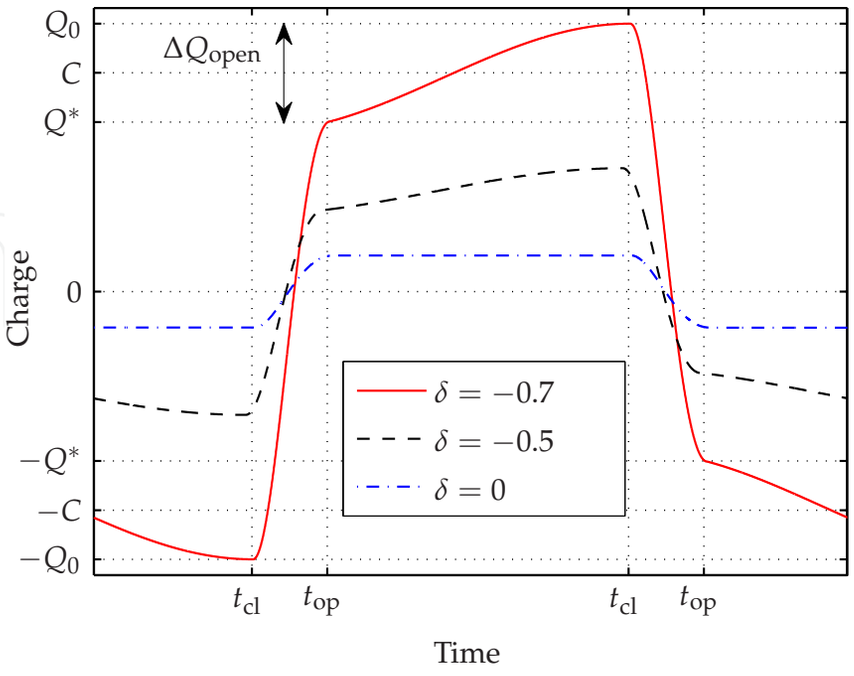

Figure 4. Time signals of the electrical charge for different capacitance values δ.

performance, can be obtained by integrating the product of piezoelectric force and mechanical velocity over a mechanical period time T_{mech},

$$E_{\mathrm{diss}} = -\alpha \int_{t^*}^{t^*+T_{\mathrm{mech}}} u_{\mathrm{p}}(t)\dot{q}(t)\,\mathrm{d}t. \tag{26}$$

When the charge inversion occurs nearly instantaneously, it is sufficient to consider the time with open switch only. With above results the piezovoltage can be obtained as

$$u_{\mathrm{p}}(t) = \frac{\alpha}{C_{\mathrm{p}}} q(t) + \frac{Q(t)}{C_{\mathrm{p}}} = \frac{\alpha}{C_{\mathrm{p}}} \frac{1}{1+\delta} q(t) + \frac{C}{C_{\mathrm{p}}}. \tag{27}$$

Inserting (27) into (26), the expression of dissipated energy is rewritten as

$$E_{\mathrm{diss}} = -\frac{\alpha}{C_{\mathrm{p}}} \int_{t^*}^{t^*+T_{\mathrm{mech}}} \left(\alpha \frac{1}{1+\delta} q(t)\dot{q}(t) + C\dot{q} \right) \mathrm{d}t = -\frac{\alpha}{C_{\mathrm{p}}} \int_{t^*}^{t^*+T_{\mathrm{mech}}} C\dot{q}\,\mathrm{d}t. \tag{28}$$

As it is shown in (28), the amount of dissipated energy only depends on the charge offset C. Therefore the aim in the design of the nonlinear shunt network is to maximize the offset of the charge. Another way to illustrate the damping performance is the hystereisis cycle, in which the piezoelectric voltage or force is drawn versus the deformation. Periodic vibrations are characterized by closed loops, and the energy dissipation is proportional to the enclosed area. Fig. 5 depicts the hysteresis loops for the standard SSDI ($\delta = 0$) and the SSDNCI with two different capacitance ratios. The voltage amplitude immediately before inversion is maximal, $\pm\hat{u}_{\mathrm{p}}$, and after inversion, $\mp\hat{u}_{\mathrm{p}}\mathrm{e}^{-\pi\zeta}$. For the case of an instantaneous voltage inversion, the hysteresis cycles are parallelograms. The slope of these lines is proportional to the force factor

α. However, for the extension of the area, only the voltage amplitude, i.e. the charge offset, is relevant. Clearly, a negative capacitance has a positive effect in both states, therefore resulting in a higher charge offset. Inserting (24) into (28) we can get the expression of the dissipated

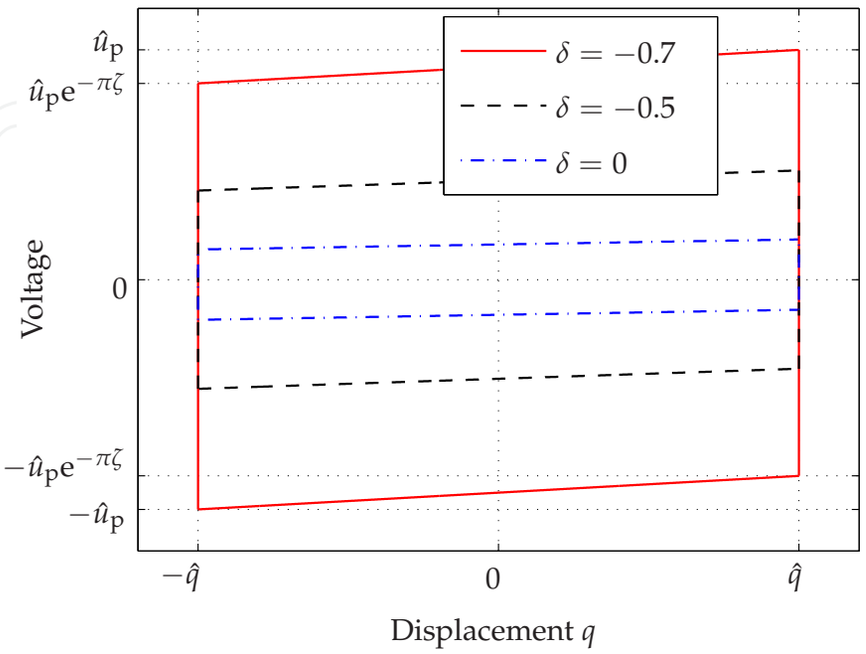

Figure 5. Hysteresis cycles for different capacitance values δ.

energy per period,

$$E_\mathrm{diss} = 4\frac{\alpha^2}{C_\mathrm{p}}\hat{q}^2\frac{1+\mathrm{e}^{-\pi\zeta}}{1-\mathrm{e}^{-\pi\zeta}}\frac{1}{1+\delta}. \tag{29}$$

The increase in dissipated energy has the same trend as for the charge offset. Comparing with SSDI shunt, the dissipated energy is scaled by $(1+\delta)^{-\frac{3}{2}}$. For a linear LRC shunt, the dissipated energy is scaled by $1/(1+\delta)$, see also in [15].

5. Optimized switching law for bimodal excitation

The assuption of a harmonic excitation is not valid for all situations. In many cases, the signal also contains additional frequencies. In order to discuss the influence of more general excitations, in the following a bimodal excitation is considered, which contains two frequencies Ω_1 and Ω_2 with $\Omega_2 > \Omega_1$,

$$q(t) = \hat{q}_1 \cos(\Omega_1 t) + \hat{q}_2 \cos(\Omega_2 t + \varphi). \tag{30}$$

Both signals have in general different amplitudes and a phase shift between them.

It is obvious that the standard switching law, which means switching at the maxima of the first mode, does not yield optimal results anymore. One can show that - using the standard switching law - the dissipated energy per vibration period is exactly the same as

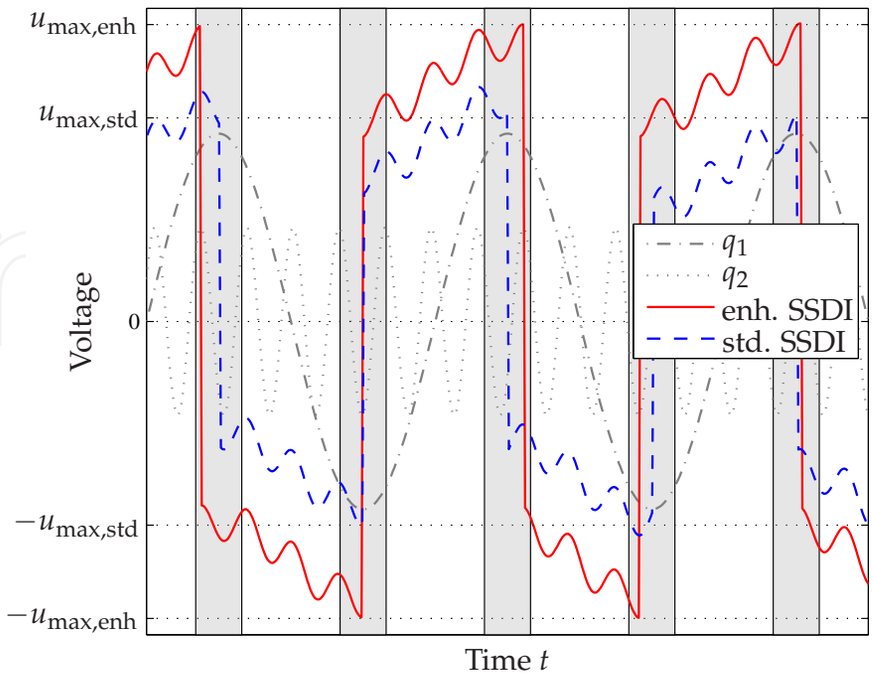

Figure 6. Time signals for standard and enhanced SSDI with bimodal excitation.

for a monoharmonic excitation with frequency Ω_1 only,

$$E_{\mathrm{diss}} = 4\frac{\alpha^2}{C_{\mathrm{p}}}\hat{q_1}^2\frac{1+\mathrm{e}^{-\pi\zeta}}{1-\mathrm{e}^{-\pi\zeta}}, \tag{31}$$

which is the result for the SSDNCI circuit with $\delta = 0$. Therefore more sophisticated switching laws have been developed, which target to extract energy from the higher frequency oscillations and use it to increase the damping of the main mode [17].

The new switching law described in the following is defined according to these positions:

- A modal observer reconstructs both vibrations in the first and second frequency of the excitation.
- A timeframe $-T_2/2 < t < T_2/2$ around each first mode extremum is defined, where T_2 is the period time of the second vibration mode. This assures that exactly one maximum and one minimum of the second mode is located within this timeframe.
- The switching is triggered at the moments of the second mode extremum. It the timeframe is defined around a maximum of the first mode, then it is triggered at the second mode maximum, if it is defined around a minimum of the first mode, then it is triggered at the second mode minimum within this timeframe.

For such a switching law it is assured that the voltage induced by the second mode is added to the value caused by the first mode. Figure 6 shows a comparison of the standard and the enhanced switching law for a biharmonic excitation. The higher frequency is recognizable

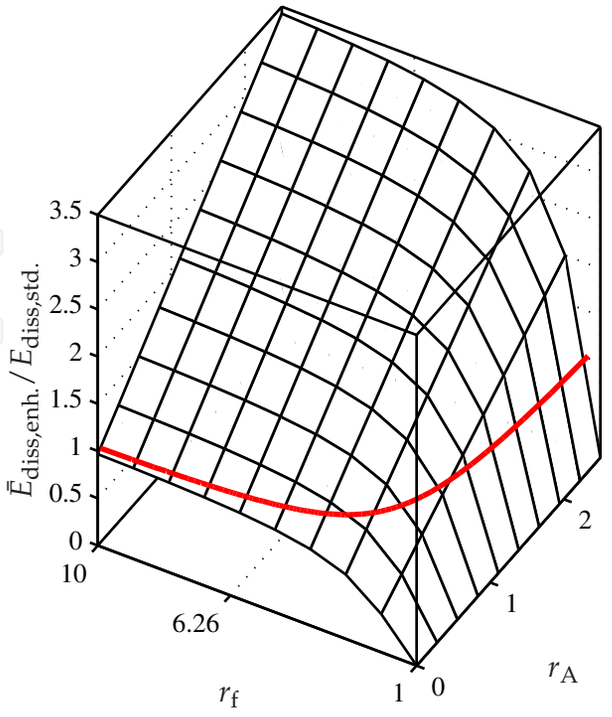

Figure 7. Amplification of dissipated energy with enhanced SSDI technique versus amplitude ratio r_{A} and frequency ratio r_{f}.

in the high frequency oscillations during the open switch phases. One can realize that in the standard switching law the switching always occurs exactly during the first mode extrema. At these moments, the voltage at the piezoceramics might be increased or decreased by the influence of the higher frequency, so that in mean this effect cancels out. With the enhanced switching law, the switch is always triggered when the second mode is maximum and augments therefore the voltage buildup. However, the switching is no longer occuring in phase with the first mode velocity, which reduces slightly the energy dissipation. For more details the reader is referred to [12].

Obviously the increase in energy dissipation grows with the second mode amplitude. But also the frequency ratio $r_{\mathrm{f}} = \Omega_2/\Omega_1$ between the first and second mode has an influence. The higher the second frequency, the smaller is the period time T_2 and therefore the timeframe. This means that the second mode maximum is in average closer to the first mode maximum, which is ideal for the energy dissipation. Figure 7 shows the amplification of energy dissipation versus the frequency ratio r_{f} and the amplitude ratio $r_{\mathrm{A}} = \hat{q}_2/\hat{q}_1$. It can be concluded that for a given frequency ratio r_{f} (this ratio is approximately $2\pi = 6.26$ for the clamped beam), the energy dissipation grows linearly with the second mode amplitude. Additionally, the energy dissipation grows with a higher second frequency. Theoretically, for very low second mode amplitude, this enhanced switching law actually might give less damping than the standard law (the borderline is marked by a red line). This is due to the non-optimal phase shift of the switching signal, which is not in exact antiphase with the first mode velocity anymore. But these regions are practically not very relevant.

6. Technical applications

After discussing the performance of various shunt damping techniques, in the following section two technical systems, namely a squealing disc brake and a bladed disc, are investigated as potential applications for piezoelectric shunt damping.

6.1 Brake squeal

Brake noise that is dominated by frequencies above 1 kHz is usually called 'brake squeal'. It is widely accepted that brake squeal is caused by friction induced vibrations. A friction characteristic that is decreasing with relative velocity results in an energy input and can excite vibrations. Other works explain the instability with nonconservative restoring forces [6, 18]. This mechanism does not need the assumption of a decreasing friction characteristic, and it is not depending on certain damping properties. Although the brake function itself is not affected by these vibrations, the generated noise marks a significant comfort problem. Brake squeal remains unpredictable, even state-of-the-art FE analyses cannot cope with the complexity of the problem. Therefore, brake manufacturers typically reduce the tendency to squeal in a time consuming process of designing, building and testing of prototypes in a mostly empirical way.

Recently, the use of piezoceramics has been investigated for the suppression of brake squeal [22] in an active feedback control. The authors succeeded in controlling the squaling, however this method requires sensing electronics, complex amplifiers and a power supply. Therefore, this technology is expensive and unsuitable for many applications like automotive brakes. Piezoelectric shunt damping for brake squeal control might be a cheaper alternative.

6.1.1 Brake prototype and stability analysis

Before designing the shunt damping network, the stability of the brake is studied using a multibody system, as shown in Figure 8. This model has been introduced in [13] to simulate

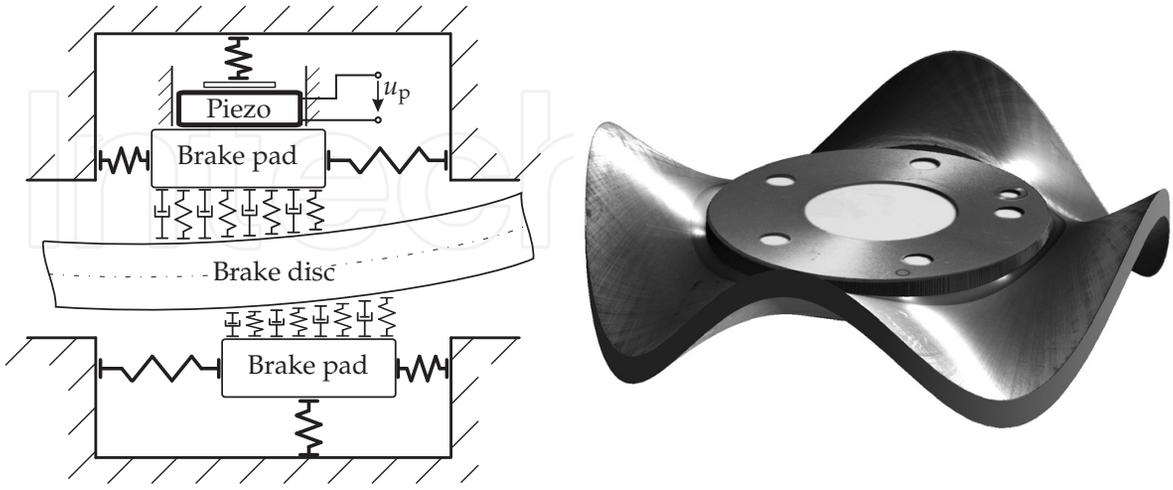

Figure 8. Brake model and disc eigenform.

the efficiency of linear *LR* and *LRC* shunts as well as a feedback control for brake squeal suppression. The two brake pads are modelled as rigid bodies and the contact area is

represented as a layer with distributed stiffness and damping properties. Both pads have two translational degrees of freedom (out-of-plane and in-plane direction) and stay in contact with the brake disc. The coefficient of friction μ between disc and pads is assumed to be constant. The brake disc is described as an annular disc according to the Kirchhoff plate theory. Only the mode with four nodal diameter and one nodal circle is considered, this mode is depicted in Figure 8, as the corresponding frequency agrees best with the squealing frequency. The rotation of the disc introduces gyroscopic terms. Further more, the brake model contains nonconservative restoring forces as a result of the friction forces in the contact area between the pads and the disc. These forces can be identified in the unsymmetric stiffness matrix. Because of these forces, the mechanical model is possibly unstable. This can be shown by a complex eigenvalue analysis, as reported in Figure 9. The stability of the brake system

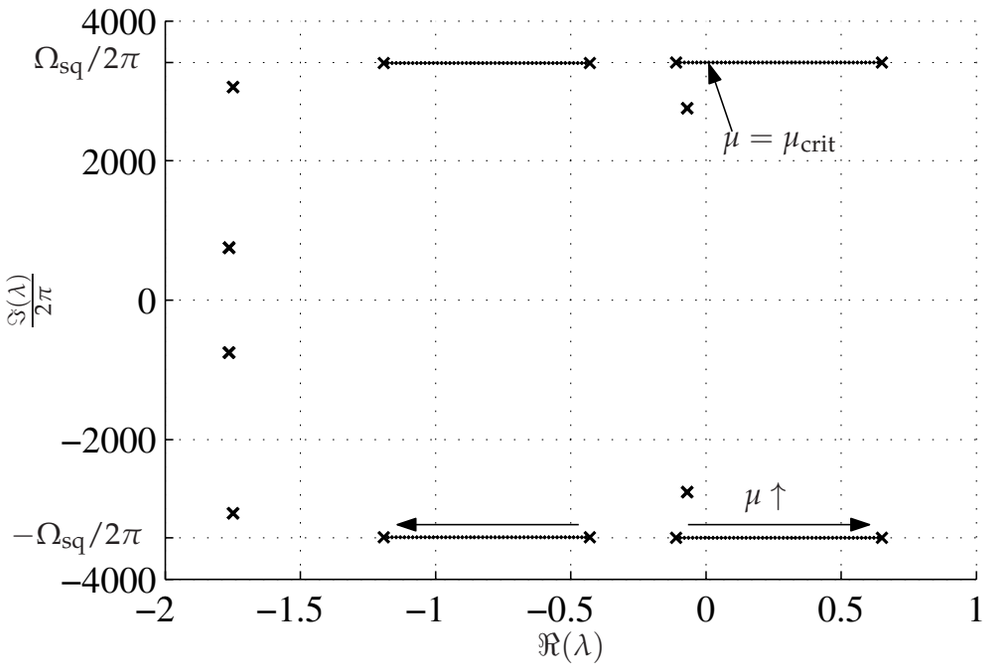

Figure 9. Imaginary part versus real part of the eigenvalues of the uncontrolled brake.

is determined by the largest real part of the eigenvalues, termed λ_{max}. A variation of the coefficient of friction μ shows the influence of the nonconservative restoring forces. Without friction forces, $\mu = 0$, the brake is asymptotically stable, as λ_{max} is negative. With increasing friction, two pairs of eigenvalues move in opposite direction. The system becomes unstable above a critical friction force μ_{crit} with $\lambda_{max}(\mu = \mu_{crit}) = 0$. The imaginary part corresponds to the squealing frequency, and is termed Ω_{sq}.

Figure 10 shows the prototype disc brake at the Institute of Dynamics and Vibration Research with three piezoelectric stack actuators. Their forces act in the same direction as the brake pressure so that the out-of-plane vibrations of the brake disc can be influenced. The piezoceramics are placed between the inboard brake pad and the brake piston and protected by a cap construction against shear forces and debris. Other publications propose a similar placement of the actuators, for example the 'smart pads' [23] which include the piezoceramics directly into the back side of the brake pads. Another possibility is to place the actuators within the brake piston [1]. Three piezoelectric stack actuators with circular cross section

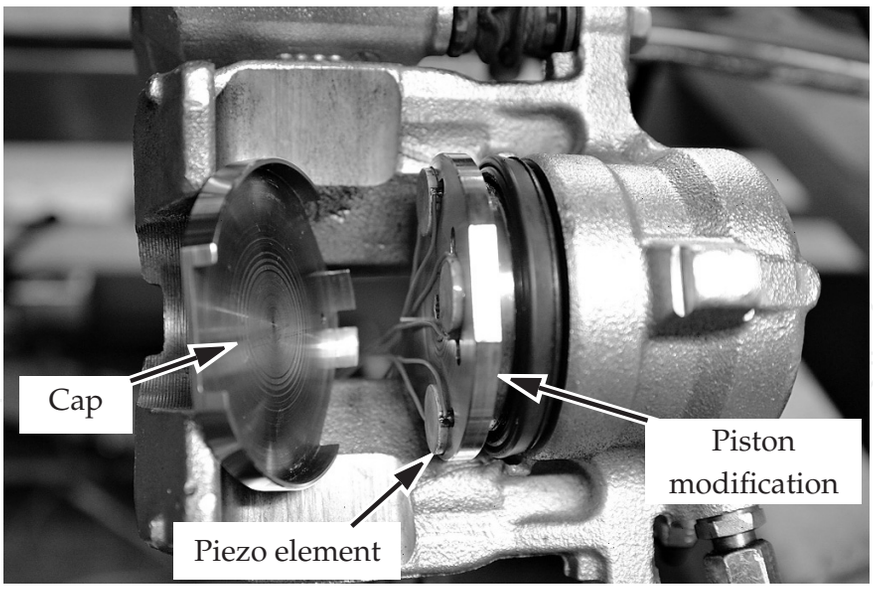

Figure 10. Prototype disc brake with embedded piezoceramics.

and material FPM 231 from company MARCO are used. They are designed to withstand brake pressures exceeding 30 bar and temperatures up to 200°C. This is certainly not enough for typical temperatures during strong brakings, but enough for principal feasibility studies in the lab. It is possible to connect all piezoceramics with *LR*- or *LRC*-shunts. When the SSDI-technique is used, one of the ceramics (typically the middle one) is used as a sensor and the remaining two are shunted.

6.1.2 Modeling of the combined system and control of brake squeal

The tuning of the resonant *LR*- and *LRC*-shunts is done like it is described in [16] for an assumed squealing frequency of $f_{\mathrm{sq}} \approx 3400\mathrm{Hz}$. The results for a passive *LR* and two negative capacitance shunts with different capacitance ratios δ are shown in Figure 11. The maximum real part $\lambda_{\max}$ is given versus the squealing frequency f_{sq}. The squealing frequency of the brake model is artificially changed by multiplicating the stiffness matrix by a constant term, which results in a change of all eigenfrequencies of the system.

All three networks are capable to stabilize the brake when tuned precisely, as $\lambda_{\max}$ is negative. However, the frequency bandwidth in which the brake is stable is very narrow for the passive *LR*-shunt. Practically this frequency range is not enough for a robust suppression of the brake squealing, as it might occur in a broad range due to the many possible eigenfrequencies of the brake. As expected, the negative capacitance networks perform better. The maximum reduction of $\lambda_{\max}$ is equal to that achievable with *LR*-networks, but this occurs in a broader frequency range. The closer the capacitance value is tuned to -1, the better the performance results.

6.1.3 Measurements on the brake test rig

Measurements are conducted on the brake test rig with the modified brake using the following procedure to experimentally determine the frequency bandwidth of the damping effect: The passive *LR* or active *LRC* shunt is disconnected from the piezoceramics, and the brake

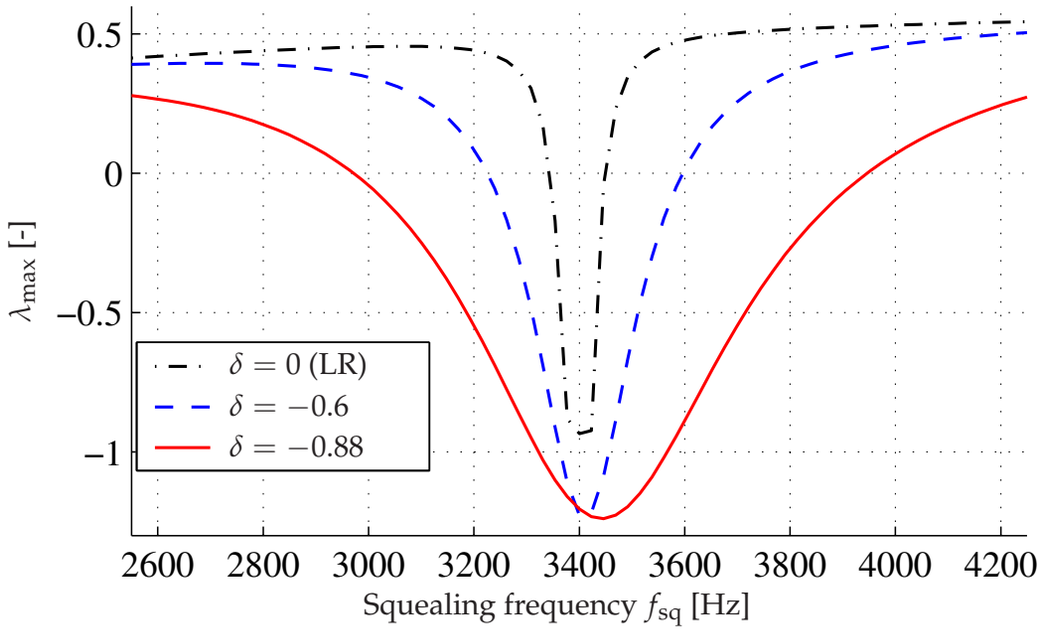

Figure 11. Stability of the brake model for LR-shunt ($\delta = 0$) and LRC-shunts with $\delta_1 = -0.6$ and $\delta_2 = -0.88$.

pressure and disc speed is varied until a proper and steady squealing arises. During the tests, this usually happens for pressures between 8 and 15 bar and velocities of 23 rpm of the beake disc. The squealing frequency could be located at approx. 3400Hz. After this, the shunt is connected to the electrodes, and the inductance and resistance are set to the calculated optimum values. Afterwards, the inductance value is reduced until the damping effect is vanishes, as the network is too strongly mistuned. This is the initial value of the inductance at the beginning of each measurement.

During the measurements, the shunt is periodically connected and disconnected for 10 seconds. After each cycle, the inductance is increased so that in the following 10 seconds of connection the shunt is tuned to a constant, new frequency. In the first half of each measurement, the electrical resonance frequency is successively tuned closer to the squealing frequency and the damping effect grows. In the middle of the measurement, the shunt is tuned nearly perfectly, and the effect is maximized. In the second half, the mistuning grows again as the inductance value is further increased, and the damping effect is diminished. The measurement is stopped when no squealing reduction is noticeable anymore. This procedure is repeated for different LR and LRC-shunts.

During the measurements, the sound pressure is recorded with a microphone, which is located in a distance of 50 cm from the brake. In the upper plot of Figure 12 the sound pressure is given versus the time for one exemplary measurement. In the lower plot, the corresponding sound pressure level (SPL) and the inductance values are shown. As shown, during the measurement time of more than 3 minutes, the SPL of the squealing brake remained nearly constant within 95-100 dB. In the very first and last switchings between connection and disconnection of the shunt, nearly no reduction in the SPL is noticed, as the mistuning is too strong. In the middle of the measurement the squealing stops immediately after connecting the shunt and starts again after disconnecting. The remaining sound without the squealing is environmental noise,

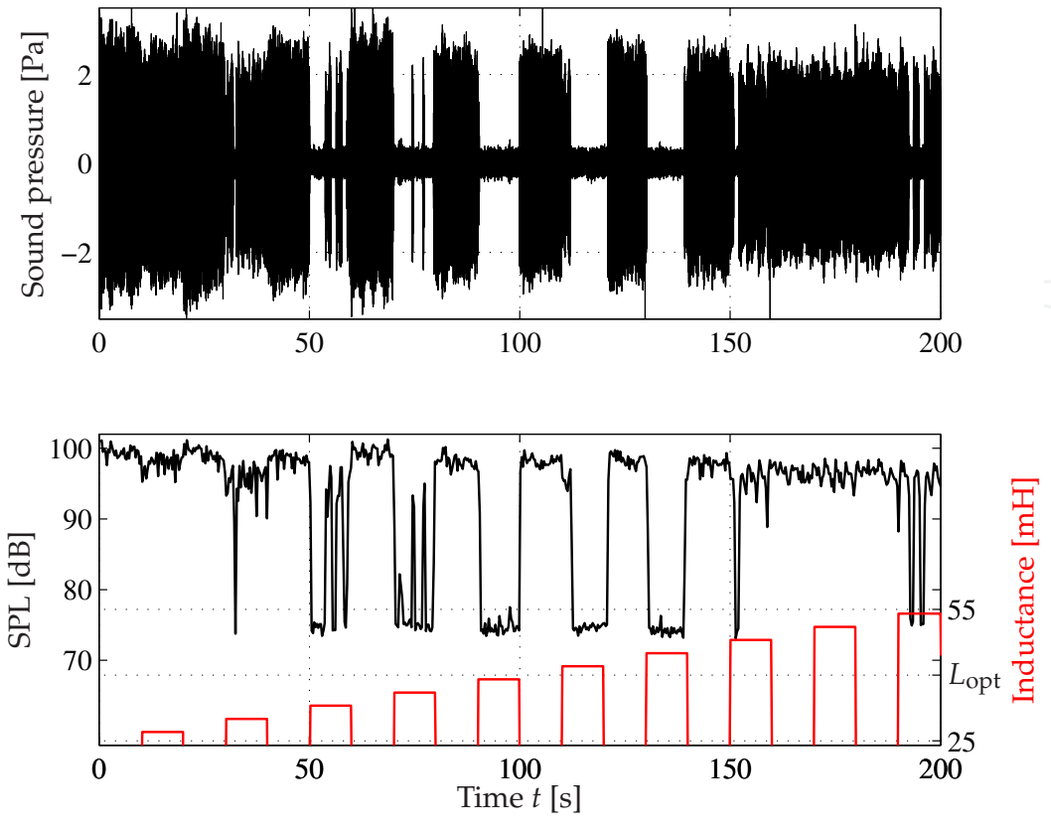

Figure 12. Sound pressure and SPL during one measurement with stepwise varied inductance.

which has been measured as high as 75 dB, and is dominated by the sound of the electric motor that drives the brake disc.

The performance of the shunted piezoceramics is evaluated by the reduction of the mean SPL during each 10 seconds of connection and disconnection for every inductance value. In Figure 13 this reduction is given versus the indunctance (normalized to the optimal value). The figure shows the results for the passive LR shunt ($\delta = 0$) and two different LRC shunts

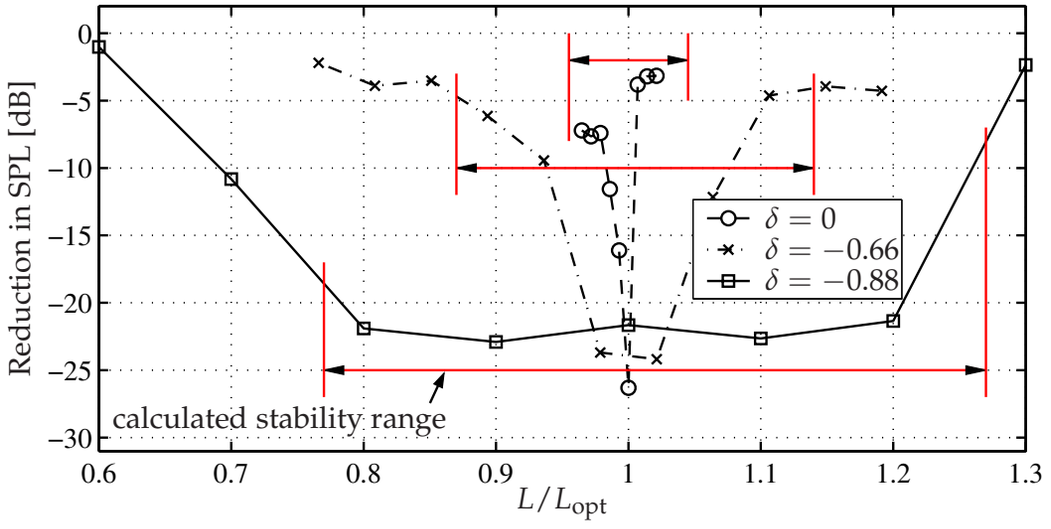

Figure 13. Reduction in SPL versus inductance tuning for LR- and LRC-shunts.

with the same capacitance ratios as in the simulations reported in Figure 11. It can be seen that the maximum reduction for each shunt is achieved for the perfectly tuned shunts ($L \approx L_{\text{opt}}$ respectively $\eta \approx 1$). In these cases, all shunts - including the passive LR shunt - are capable to suppress the squealing totally, as predicted by the simulations. The differences in the maximum reduction can be explained by different strength of the squealing. Naturally, a weak squealing delimits the maximum possible reduction compared to a strong squealing.

From the inductance ratio L/L_{opt}, the frequency ratio between the electrical eigenfrequency and the squealing frequency can be re-calculated. Defining the state 'silent' and 'squealing' by an arbitrary threshold of 12 dB SPL-reduction, the brake is stabilized in a range of $\Delta f = 40$Hz for the passive LR shunt. With actice LRC-shunts, the stabilized range covers $\Delta f = 212$Hz with $\delta = -0.66$ and $\Delta f = 950$Hz with $\delta = -0.88$. These results show a good accordance with the simulation results in Figure 11. However, some influences like the heating up of the piezoceramics lead to a reduction of the piezoelectric effect so that the performance at the end of each measurement is slightly lower than in the beginning.

6.2 Damping of turbine blades

Another application is the vibration damping of turbine blades. Here the excitation comes from high static and dynamic loads. Static loads are due to centrifugal forces and thermal strains while fluctuating gas forces are the cause of dynamic excitation which can lead to High Cycle Fatigue (HCF) failures. As the material damping is extremely low, any further damping provided to the structure is desireable. Coupling devices like underplatform dampers, lacing wires and tip shrouds are common in turbomachinery applications [19, 20]. The effectiveness of these damping concepts is limited to the relative vibrations of neighbouring blades and therefore they are often only efficient for specific engine speeds and mode shapes. Furthermore, the aerodynamics of the blades is influenced by these coupling devices.

In the following, the damping of turbine blades by shunted piezoceramics is studied with a bladed disc model (BLISC), depicted in Figure 14, which has been introduced by Hohl [8]. Each

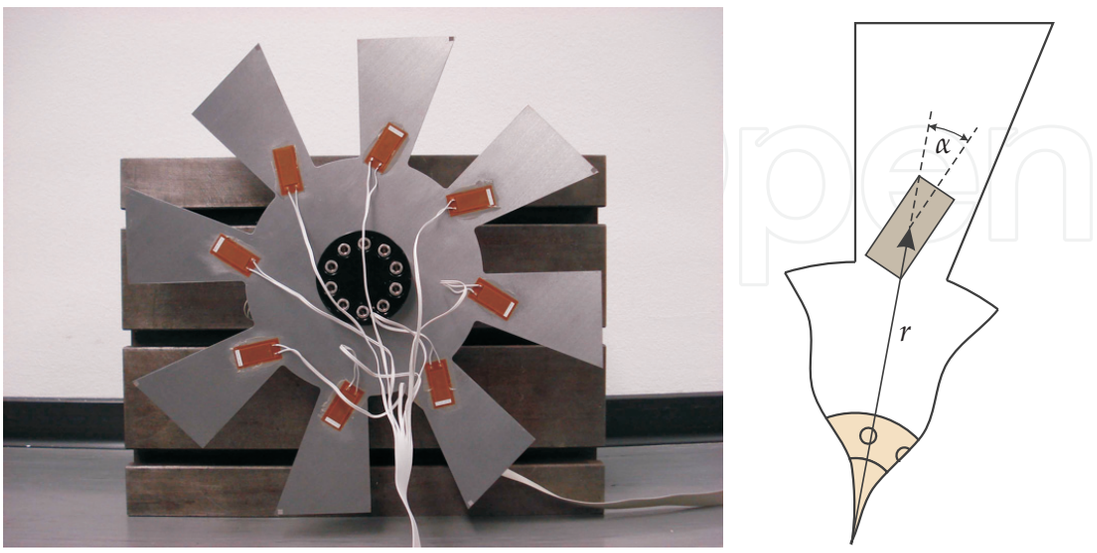

Figure 14. Photography and sketch of the BLISC test rig with attached piezoceramics.

blade is equipped with a MACRO FIBER COMPOSITE piezoceramics M2814 P1 from MARCO company for vibration damping.

6.2.1 Optimizing the location of the piezoceramics

The intention of this study was to optimize the placement of the piezoceramics within the structure. As the geometry is too complex for an analytical description, it is modeled by Finite Elements in Ansys using 3-D 20-Node structural solid elements (solid186) and a 3-D 20-node coupled-flied solid (solid226) for the piezoelectric material. Subsequently a modal reduction is performed. The location of every piezoceramics is described by the radius r and the orientation α, which have to be optimized, with the generalized coupling coefficient K taken as a measure of the coupling. This factor can be calculated by the system' eigenfrequencies with isolated and short circuit electrodes of the piezoceramics, which are both determined within the FE program. Generally, the coupling with the individual eigenforms of the system differ from each other. In Figure 15 the coupling coefficients for the first bending and first torsion mode of the blades are given versus α and r. For the bending mode, the piezoceramics should

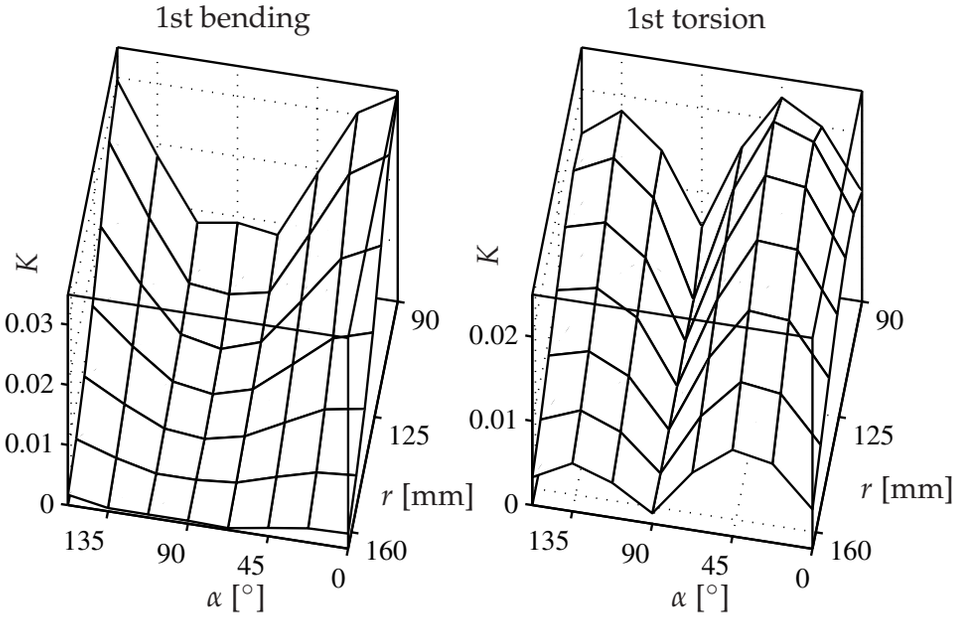

Figure 15. Generalized coupling coefficient K for the first bending and torsion modes versus the location of the piezoceramics.

be placed close to the clamped ending of the blade at $r = 90$mm, which is approximately the radius of the disc. This can be explained by the bending moment, which is maximized at this position. The bending moment reduces to zero at the free end of the blade, therefore also the coupling reduces in that direction. The dependency with the orientation α is nearly symmetric: the coupling is maximal when the piezoceramics is facing in radial direction ($\alpha = 0°$ or $\alpha = 180°$) and minimal for $\alpha = 90°$. The resulting maximum coupling is $K \approx 3.5\%$.

For the torsion mode, the optimal radius is similar, yet slightly larger than for the bending mode. However, the orientation is oppositional to the bending case: the best coupling results for $\alpha = 45°$, while it is nearly zero for $\alpha = 0°$ and $\alpha = 90°$. The maximum coupling with the torsion mode is $K \approx 2.25\%$ and thus smaller than for the bending.

Therefore, for the overall optimal location a trade-off is necessary, and the piezoceramics is placed with $r = 97.5\text{mm}$ and $\alpha = 22.5°$. In this case the coupling with both the bending and torsion mode is about $K = 2\%$.

6.2.2 Measurements

Finally, measurements are conducted with the BLISC test rig. The system is excited harmonically by additional piezoceramics placed at the back side at identical positions as the shunted ones at the front side. One single passive *LR* network is connected to all piezoceramics simultaneously, and the electrical eigenfrequency and the damping ratio are set to the optimal values according to the previous sections. Figure 16 shows the measurement as well as the simulation results for isolated electrodes and optimal *LR*-shunting. Generally, the

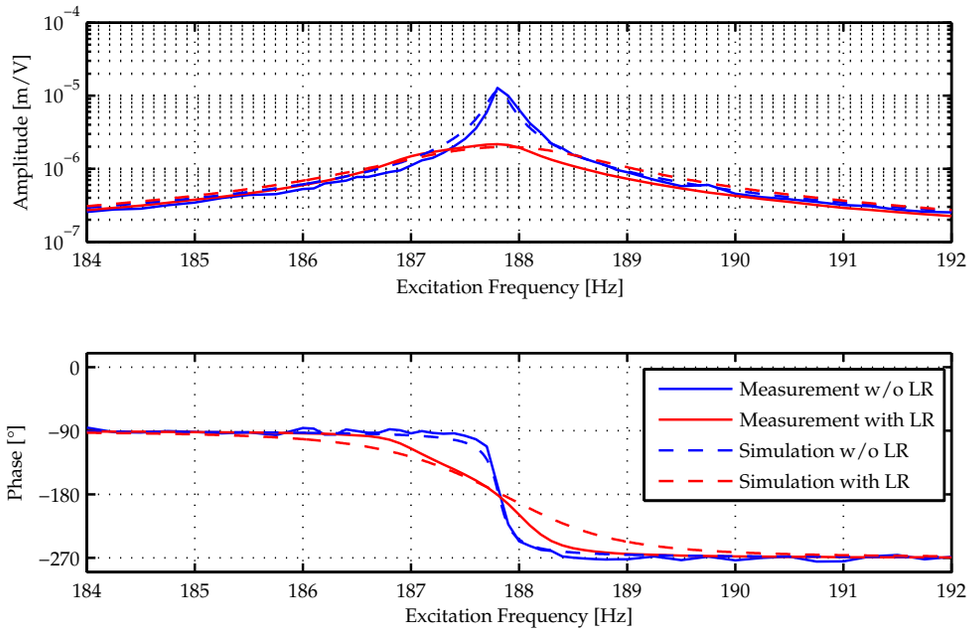

Figure 16. Simulated and measured frequency response of the BLISC model for isolated electrodes and *LR*-shunting.

simulation results are in very good agreement with the measured ones. The damping effect of the shunted piezoceramics is clearly visible.

7. Conclusions

This chapter deals with shunted piezoceramics for vibration damping. A small overview of typical shuntings is presented. Further on, a general model of a one degree of freedom mechanical oscillator with embedded piezoceramics and external electrical circuit is derived.

Based on this system, the optimal tuning of a resonant *LR*-shunt is performed for a damped mechanical system. The influence of the mechanical damping upon the optimal parameters and the resulting damping performance is studied. Further on, a novel combination of a 'SSDI' switching circuit and a negative capacitance is discussed. It is shown that this network

inherits the adaptive structure of the SSDI technique and combines it with the enhanced performance of a negative capacitance. An enhanced switching law for bimodal excited systems is presented as well. With this technique, the damping of the main mode can be maximized using the vibration energy stored in the higher mode.

Finally, a squealing disc brake and a bladed disc are introduced as two technical applications for piezoelectric shunt damping. For both cases the vibration behavior is studied by mechanical replacement models, and the location of the piezoceramics and the electrical shuntings are chosen based on these models. In both cases it is possible to control the vibrations and increase significanly the damping of the structure. Measurements are conducted which validate the theoretical models.

Author details

Marcus Neubauer, Sebastian M. Schwarzendahl and Xu Han
Institute of Dynamics and Vibration Research, Leibniz University Hannover, Germany

8. References

[1] Cunefare, K. A. & Graf, A. J. [2002]. Experimental active control of automotive disc brake rotor squeal using dither, *Journal of Sound Vibration* 250: 579–590.

[2] Fleming, A. J., Behrens, S. & Moheimani, S. O. R. [2003]. Reducing the inductance requirements of piezoelectric shunt damping systems, *Smart Material Structures* 12: 57–64.

[3] Forward, R. L. [1979a]. Electromechanical transducer-coupled mechanical structure with negative capacitance compensation circuit.
URL: *http://www.freepatentsonline.com/4158787.html*

[4] Forward, R. L. [1979b]. Electronic damping of vibrations in optical structures, *Applied Optics* 18: 690–697.

[5] Fukada, E., Date, M., Kimura, K., Okubo, T., Kodama, H., Mokry, P. & Yamamoto, K. [Apr 2004]. Sound isolation by piezoelectric polymer films connected to negative capacitance circuits, *Dielectrics and Electrical Insulation, IEEE Transactions on [see also Electrical Insulation, IEEE Transactions on]* 11(2): 328–333.

[6] Hagedorn, P. [2003]. Modeling disk brakes with respect to squeal, *COBEM*.

[7] Hagood, N. W. & von Flotow, A. [1991]. Damping of structural vibrations with piezoelectric materials and passive electrical networks, *Journal of Sound Vibration* 146: 243–268.

[8] Hohl, A., Neubauer, M., Schwarzendahl, S. M., Panning, L. & Wallaschek, J. [2009]. Active and semiactive vibration damping of turbine blades with piezoceramics, Vol. 7288, SPIE, p. 72881H.
URL: *http://link.aip.org/link/?PSI/7288/72881H/1*

[9] Hollkamp, J. J. [1993]. Multimodal passive vibration suppression with piezoelectrics, *in* R. B. Malla & B. B. Nalluri (eds), *AIAA/ASME/ASCE/AHS/ASC Structures, Structural Dynamics, and Materials Conference, 34th and AIAA/ASME Adaptive Structures Forum, La Jolla, CA, Apr. 19-22, 1993, Technical Papers. Pt. 6 (A93-33876 13-39), p. 3227-3237.*, pp. 3227–3237.

[10] Lefeuvre, E., Badel, A., Petit, L., Richard, C. & Guyomar, D. [2006]. Semi-passive Piezoelectric Structural Damping by Synchronized Switching on Voltage Sources, *Journal of Intelligent Material Systems and Structures* 17(8-9): 653–660.
URL: *http://jim.sagepub.com/cgi/content/abstract/17/8-9/653*

[11] Mokrani, B., Rodrigues, G., Ioan, B., Bastaits, R. & Preumont, A. [2012]. Synchronized switch damping on inductor and negative capacitance, *Journal of Intelligent Material Systems and Structures* .

[12] Neubauer, M., Han, X. & Schwarzendahl, S. M. [2011]. Enhanced switching law for synchronized switch damping on inductor with bimodal excitation, *Journal of Sound and Vibration* 330(12): 2707 – 2720.
URL: *http://www.sciencedirect.com/science/article/B6WM3-520V42F-3/2/9fea46dd56c528bf824c8190fb0d1b95*

[13] Neubauer, M. & Kroeger, M. [2006]. Suppression of brake squeal using piezoceramics, *Braking 2006: International Conference on Vehicle Braking Technology*, pp. 254–263.

[14] Neubauer, M. & Wallaschek, J. [2008]. Analytical and experimental investigation of the frequency ratio and switching law for piezoelectric switching techniques, *Smart Materials and Structures* 17(3): 035003 (9pp).
URL: *http://stacks.iop.org/0964-1726/17/035003*

[15] Neubauer, M. & Wallaschek, J. [2009]. Vibration damping with piezoceramics shunted to negative capacitance networks, *Proceedings of International Conference on Advanced Intelligent Mechatronics, Singapore*, pp. 1100–1105.

[16] Neubauer, M. & Wallaschek, J. [2010]. Vibration Damping with Shunted Piezoceramics: Fundamendals and Technical Applications, Presented at the 6th Int. Conference Mechatronic Systems and Materials (MSM).

[17] Richard, C., Harari, S. & Gaudiller, L. [2009]. Enhanced piezoelectric voltage build-up for semi-active control of smart structures, Vol. 7288, SPIE, p. 72881Y.
URL: *http://link.aip.org/link/?PSI/7288/72881Y/1*

[18] Rudolph, M. & Popp, K. [2001]. Brake squeal, *in* K. Popp (ed.), *Detection, Utilization and Avoidence of Nonlinear Dynamical Effects in Engineering Applications*, Shaker Verlag, pp. 197–225.

[19] Sextro, W. [2000]. The calculation of the forced response of shrouded blades with friction contacts and its experimental verification, ASME Paper 2000-GT-540, Int. Gas Turbine & Aeroeng. Congress & Exh., Munich.

[20] Szwedowicz, J. [1999]. Cyclic Finite Element Modeling of Shrouded Turbine Blades Including Frictional Contacts, ASME Paper 99-GT-92, Int. Gas Turbine & Aeroeng. Congress & Exh., Indianapolis.

[21] Tang, J. & Wang, K. W. [2001]. Active-passive hybrid piezoelectric networks for vibration control: comparisons and improvement, *Smart Material Structures* 10: 794–806.

[22] von Wagner, U., Hochlenert, D., Jearsiripongkul, T. & Hagedorn, P. [2004a]. Active control of brake squeal via 'smart pads'.

[23] von Wagner, U., Hochlenert, D., Jearsiripongkul, T. & Hagedorn, P. [2004b]. Active control of brake squeal via smart pads, *SAE 2004 Transactions Journal of Passenger Cars - Mechanical Systems* pp. 1186–1192.